

Thermoelectric $\text{Ca}_{0.9}\text{Yb}_{0.1}\text{MnO}_{3-\delta}$ grain growth controlled by spark plasma sintering

Simon Quétel-Weben^{a,*}, Richard Retoux^a, Jacques G. Noudem^{a,b}

^a CRISMAT, UCBN, 6Bd Maréchal Juin, 14050 Caen Cedex 4, France

^b LUSAC, UCBN, rue Aragon, 50130 Cherbourg, France

Received 5 September 2012; received in revised form 28 January 2013; accepted 4 February 2013

Available online 16 March 2013

Abstract

n-Type $\text{Ca}_{0.9}\text{Yb}_{0.1}\text{MnO}_{3-\delta}$ thermoelectric (TE) powders were prepared by solid state synthesis (SSS) and co-precipitation method (Cop). The bulk TE materials were consolidated using conventional sintering (CS) and spark plasma sintering (SPS) respectively. The shrinkage behavior, as well as the sample densification strongly depends on the starting particle size. Consequently, the bulk samples from normal powder (SSS) and nano-powder (Cop) were prepared with similar density by using different sintering temperatures, of 1400 °C and 1200 °C, then 1200 and 950 °C for CS and SPS respectively. Such a decrease (up to 200 °C) of the sintering temperature is a consequent progress in terms of engineering for applications. Another advantage of the co-precipitation process compared to the conventional solid state synthesis is that, due to the small particle sizes and the decreased sintering temperature, grain growth was limited and TE properties were enhanced. The interest of the SPS process was also evidenced and we are presenting here the structural and microstructural investigations. In addition, the thermoelectric properties of samples prepared with two different processes were studied with the figure of merit of 0.18 at 750 °C.

© 2013 Elsevier Ltd. All rights reserved.

Keywords: Calcium manganites; Soft chemistry synthesis; Thermoelectric oxides; Ceramics; Spark plasma sintering; Grain growth

1. Introduction

The 2011 United Nations Framework Convention on Climate Change Conference (UNFCCC) was held in Durban (South Africa), from 28 November to 11 December 2011. One more time, this meeting demonstrated the emergency to protect our environment against global warming by limiting carbon emissions. Saving energy could be one of the key issues and the possibility of creating electricity from waste heat by using thermoelectric (TE) materials for generators has been demonstrated.^{1–3} To design an efficient TE generator it is necessary to find materials with promising performance, which can

be evaluated by the so-called figure of merit, Z , defined as $S^2/\rho\kappa$, where S , ρ and κ are respectively the Seebeck coefficient, electrical resistivity and thermal conductivity. The discovery of oxide materials⁴ with large thermopower, S , has renewed interest in these materials. In contrast to conventional intermetallics such as SiGe, Bi_2Te_3 ,^{5,6} thermoelectric oxides particularly exhibit a potential to resist to oxidation or decomposition at high temperature ($T > 700$ K). Since the first report on thermoelectric oxide, NaCo_2O_4 ,⁴ various new *n* and *p*-type oxide materials having high performance and environmental stability at high temperatures have been reported.^{7–11} For *n*-type, various compounds seem to have potential such as $(\text{In},\text{Ge})_2\text{O}_3$,¹⁰ SrTiO_3 ,¹¹ ZnO ¹² and/or CaMnO_3 ¹³ wherein Ca^{2+} is partially replaced by trivalent rare earth cations^{8,14} in order to induce *n*-type conductivity and likely to enhance its thermoelectric behavior. Furthermore, the substitution of the Ca site with a trivalent cation will increase the carrier concentration and generate Mn^{3+} cations in the Mn^{4+} matrix, changing the strength of the bending of the Mn–O–Mn bond as reported elsewhere.¹⁵

On the one hand, this paper deals with the temperature densification effect due to the different starting powder on the ceramic materials prepared by both conventional and spark

Abbreviations: cop, coprecipitation; CS, conventional sintering; DSC, differential scanning calorimeter; ED, electron diffraction; EDX, energy dispersive X-ray spectroscopy; LFA, laser flash analyzer; SEM, scanning electron microscopy; SPS, spark plasma sintering; SSS, solid state sintering; TE, thermoelectric; TGA, thermo gravimetric analysis; TMA, thermo-mechanical analysis; XRD, X-rays diffractometers.

* Corresponding author. Tel.: +33 2 31 45 13 77; fax: +33 2 31 45 13 09.

E-mail addresses: simon.quetel-weben@ensicaen.fr, simon.qwd@gmail.com (S. Quétel-Weben).

plasma sintering processes. On the other hand, thermoelectric properties, structure analyses and microstructure developed and investigated by both scanning and transmission electron microscopy (SEM, TEM) are discussed.

2. Experimental procedure

2.1. Synthesis

The *n*-type thermoelectric oxide with $\text{Ca}_{0.9}\text{Yb}_{0.1}\text{MnO}_3$ formulation was synthesized using two routes, the conventional solid state synthesis (SSS) and the co-precipitation method (COP), as described elsewhere.¹⁶ Various compounds such as calcium carbonate (CaCO_3 , 99.99% pure), manganese carbonate (MnCO_3 , 99.9%) and ytterbium nitrate ($\text{Yb}(\text{NO}_3)_3 \cdot x\text{H}_2\text{O}$, 99.99%) were used as precursors, Hydrate content of ytterbium nitrate ($\text{Yb}(\text{NO}_3)_3 \cdot 5.45\text{H}_2\text{O}$) was determined by TGA measurements using a Netzsch (STA 449 F3 Jupiter) device.

All the compounds were mixed in water, after stirring and heating at 80 °C, a solution of nitric acid (HNO_3) 65% wt was added to dissolve the cation precursors; a few drops of hydrogen peroxide (H_2O_2) were also added in order to prevent manganese oxidation. Ammonium carbonate ($(\text{NH}_4)_2\text{CO}_3$) was dissolved in distilled water, which would serve as the precipitant solution. The co-precipitation process started by adding the cooled nitrate stock solution into the precipitant solution and was followed by a 2 h stirring. The resultant suspension was subjected to centrifugation. Finally, the dried material was heated at 850 °C for 6 h in air.

2.2. Sintering

The samples of 8 mm diameter were previously pelletized using 500 MPa uniaxial pressure. The green densities of 2.94 and 2.51 g cm⁻³ were measured for the samples pressed respectively from the solid state synthesis and co-precipitation powders. These relative densities were deduced from the ratio of mass over volume of the sample. Details of the different samples prepared in the framework of this study are reported in Table 1.

Thermo-mechanical analyses (TMA) were done using a SETARAM Setsys (Caluire, France) in order to determine the optimal sintering temperature of the sample used. The TMA measurements show (Fig. 1) that the shrinkage behavior and the sintering temperature strongly depend on the starting particle size. The shrinkage of 19% of fine co-precipitated powder is achieved at 1150 °C. As for the solid state synthesis, shrinkage

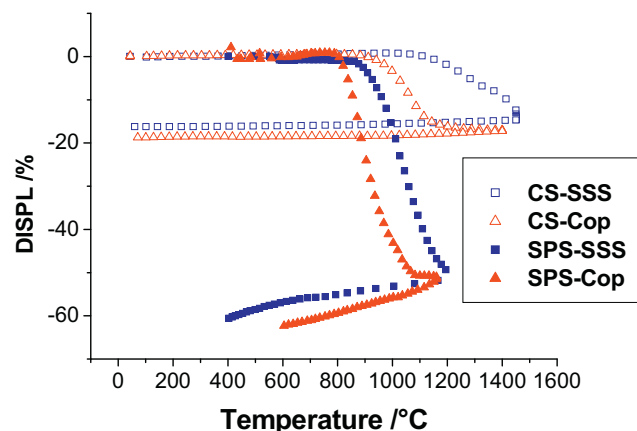


Fig. 1. TMA measurements of samples made by solid state synthesis (blue square) and co-precipitation way (red triangle), by conventional sintering (open symbols) and SPS (filled symbols). (For interpretation of the references to color in the artwork, the reader is referred to the web version of the article.)

is not completed at 1400 °C (16%) (near the limit of SETARAM experimental device). According to these thermal expansion measurements the sintering temperatures of 1400 and 1200 °C were deduced when the starting powders were SSS and COP respectively. Other samples were sintered by spark plasma sintering (SPS).

The FCT-HP D25 (Rauenstein, Germany) machine was used in DC mode with a maximal power of 8 kW, a heating and cooling rate of 100°/min, and a pressure of 50 MPa. To control grain growth, different sintering temperatures from 900 to 1050 °C and dwell time from 5 min to 3 h were investigated with the coprecipitation-prepared powder. A graphite protective film was inserted between the powder and the 15 mm diameter graphite matrix. The FCT device offers the possibility to monitor the sample displacement (Fig. 1). Uniaxial shrinkage at low temperature is close to 65% for co-precipitation powder compared to 50% for SSS. The optimal sintering temperatures for SPS are found around 950 °C and 1200 °C for co-precipitation and solid state synthesis powders respectively. The samples sintered by SPS show higher displacements, probably due to the die stresses. In the case of SPS, densification occurs in one direction while in the conventional TMA, shrinkage is commonly in every direction. But we can also point out that, in the case of SPS, the starting material is a non-pressed powder whereas it is a preformed pellet for the TMA process. The bulk samples obtained after SPS consolidation were first polished to remove the graphite foil and then annealed at 800 °C during 12 h under air, in order to re-oxidize the material.

The sintering temperatures and the initial and final densities are summarized in Table 1. On the one hand, from the thermal expansion curves, the sintering temperatures of 1400 and 1200 °C have been deduced for conventional sintering (CS) when the initial powders are SSS and COP respectively. On the other hand, temperatures of 1200 and 950 °C were used in the case of spark plasma sintering (SPS). Thereafter, we will name CS1, CS2, SPS1 and SPS2 the samples processed at these four temperatures and using respectively solid state synthesis (SSS) and co-precipitation (COP) powders.

Table 1
Samples characteristics.

	CS1	CS2	SPS1	SPS2
Synthesis method	SSS	COP	SSS	COP
Sintering method	CS	CS	SPS	SPS
Sintering temperature (°C)	1400	1200	1200	950
Initial (g cm ⁻³)	2.94(4)	2.51(4)		
Final (g cm ⁻³)	4.58(5)	4.75(5)	4.377(5)	4.72(6)
Relative density	92.2%	95.2%	87.7%	94.7%

2.3. Characterization

The samples densities were determined by the Archimedes method with a Kern ABT 220–4 M analytical balance and checked by the helium pycnometry process with a Micromeritics AccuPyc 1330 pycnometer. X-ray powder diffraction patterns were recorded on an X'PERT (Almelo, Netherlands) Pro MPD PANalytical powder diffractometer in Bragg–Bretono configuration. The X-ray diffraction (XRD) of starting co-precipitated powder was performed for phase identification and a D8 Advance Vario1 Bruker diffractometer (Billerica, MA, USA) was used for XRD temperature scanning from 400 to 900 °C, with a 25 °C step. For each temperature, the data were collected for 2θ varying from 15° to 80° during 1.3 s per 0.0157°. X'pert Highscore was used for phase matching and Jana2006 for parameter refinement. A Carl Zeiss Supra 55 (Oberkochen, Germany) high resolution scanning electron microscope (SEM) equipped with an EDAX EDX analyzer was used to investigate the microstructure and the chemical composition of the samples after processing. Specimens for the transmission of electron microscopy (TEM) observations were prepared by crushing the SPS2 sample in ethanol. After dispersion of the crystallites, a drop of the suspension was deposited and dried onto a carbon-coated copper grid. The TEM study was performed using a 200 kV JEOL 2010 FEG transmission electron microscope fitted with a double tilt sample holder (tilts $\pm 42^\circ$). As in SEM studies the cationic composition of the materials was determined by energy dispersive X-ray analysis (EDX) using an EDAX analyzer coupled with the microscope.

The manganese oxidation state was investigated by back titration with iron sulphate salt (Mohr salt), under argon atmosphere.

Thermal diffusivity was determined with a Netzsch LFA 457 Microflash device, and the specific heat with a DSC measurement with another Netzsch system (STA 449 F3 Jupiter Selb, Germany).

Thermal conductivity was then deduced from the formula:

$$\kappa(T) = C_p(T) \times d \times \alpha(T)$$

where κ is the thermal conductivity, C_p the heat capacity, d is the sample density and α thermal diffusivity. In this study, we assume that d is almost constant in the given temperature range. The specific heat of $\text{Ca}_{0.9}\text{Yb}_{0.1}\text{MnO}_{3-\delta}$ was measured with the value around $0.699 \text{ J g}^{-1} \text{ K}^{-1}$ in the whole range of temperature.

Finally, the electrical resistivity, ρ , and Seebeck coefficient, S , were measured simultaneously by the dc four-probe method by using a ZEM-3 (ULVAC-RIKO, Inc, Japan) from room temperature to 750 °C. Errors on the measurements by using this device are approximately 5%.

3. Results and discussion

3.1. X-rays diffraction analysis

Fig. 2 shows the phase development of $\text{Ca}_{0.9}\text{Yb}_{0.1}\text{MnO}_{3-\delta}$ from the coprecipitation powder. The aim of this study is to define the optimal temperature of calcination in order to prevent grain growth before the processing stage.

X-ray analysis of the powder synthesized by co-precipitation (Fig. 2) illustrates one crystalline phase $\text{CaMn}(\text{CO}_3)_2$ from 400 to about 600 °C. The cell volume deduced is 208.3 Å and can be compared to the referenced cell¹⁷ that has a volume of 207,533 Å. We can therefore assume that the rare earth atom

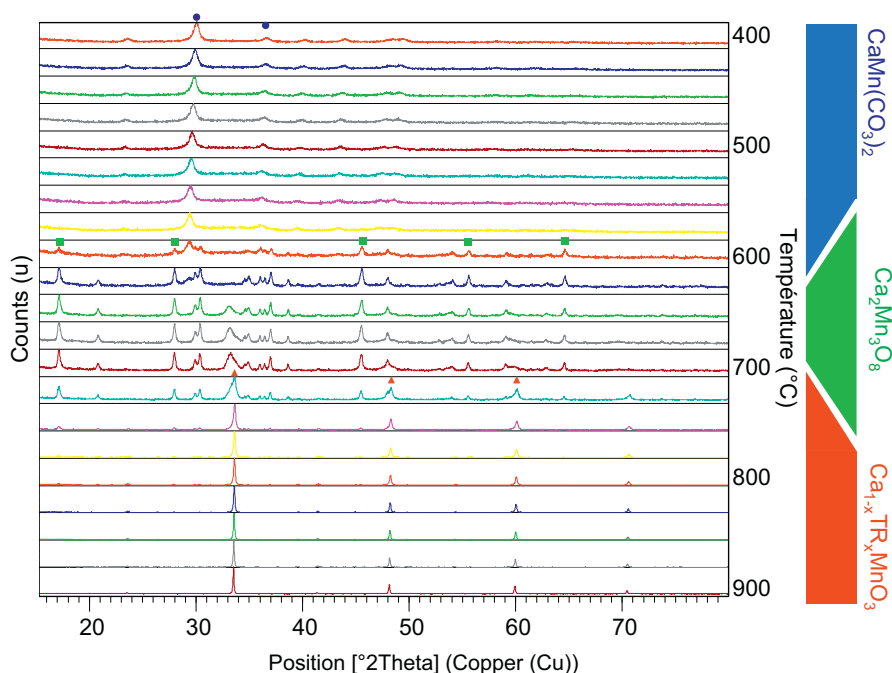


Fig. 2. XRD patterns of coprecipitation powder before calcination, from 400 to 900 °C, main peaks are marked; (●) $\text{CaMn}(\text{CO}_3)_2$, (■) $\text{Ca}_2\text{Mn}_3\text{O}_8$, (▲) $\text{Ca}_{0.9}\text{Yb}_{0.1}\text{MnO}_3$. (For interpretation of the references to color in the artwork, the reader is referred to the web version of the article.)

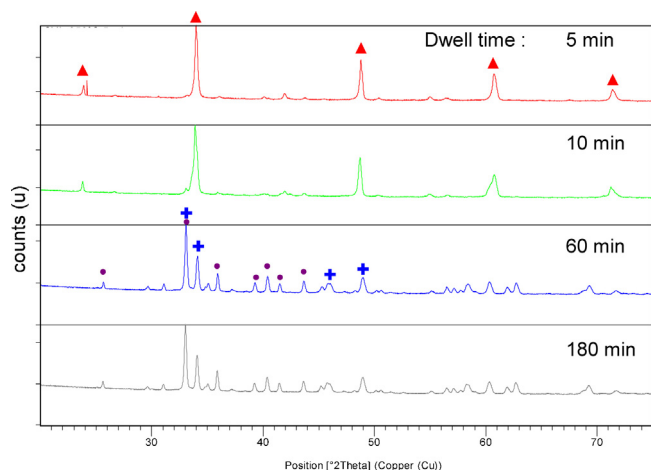


Fig. 3. XRD patterns of samples made by coprecipitation and sintered by SPS at 950 °C, at different dwell time (5, 10, 60 and 180 min). Mains peaks are marked: (▲) $\text{Ca}_{0.9}\text{Yb}_{0.1}\text{MnO}_3$, (●) CaMn_2O_4 , (+) $\text{Ca}_2(\text{MnO}_4)$. (For interpretation of the references to color in the artwork, the reader is referred to the web version of the article.)

is inserted in the crystal cell. EDS analysis confirms the Yb substitution in the lattice with an Yb/Mn ratio around 1/10, depending on the analyzed zone. However, the ratio can differ about 20%.

The compound $\text{CaMn}(\text{CO}_3)_2$ gradually disappears with the appearance of a new oxide compound, $\text{Ca}_2\text{Mn}_3\text{O}_8$, between 600 and 725 °C. One can note that the formation of the $\text{Ca}_{1-x}\text{TR}_x\text{MnO}_{3-\delta}$ compound starts around 725 °C and becomes single-phased at 800 °C. Fig. 3 shows the XRD patterns of the SPS samples processed at 950 °C under 50 MPa at different dwell time ($t = 5, 10, 60$ and 180 min). When the dwell time is lower than 10 min, the single phase is identified. We can clearly observe that above 10 minutes a mixture of CaMn_2O_4 and $\text{Ca}_2(\text{MnO}_4)$ is evidenced. One can note that the samples processed at a temperature higher than 950 °C also show these two oxide compounds.

3.2. Electron diffraction

Numerous crystals from sample SPS2 were investigated using the Selected Area Electron Diffraction (SAED) method. On every electron diffraction pattern recorded, the main spots could be indexed using the classical $a = 5.28 \text{ \AA}$; $b = 7.46 \text{ \AA}$; $c = 5.27 \text{ \AA}$ Pnma cell parameters of the parent compound CaMnO_3 . These parameters are in good agreement with the XRD results presented in Table 2, showing the small cell expansion of $\text{Ca}_{0.9}\text{Yb}_{0.1}\text{MnO}_3$. At this point, it is important to notice that on a lot of electron diffraction patterns, along the main crystallographic directions of the structure, extra spots can be evidenced between the main spots characteristic of the CaMnO_3 type structure. Such a typical ED pattern is presented in Fig. 4 (010 × orientation). We can deduce from this ED pattern that the extra spots are representative of two main phenomena occurring in the SPS treated samples. First a large number of crystals presents boundaries involving 90°-oriented domains, secondly, in most cases in these twinned crystals the periodicity of the extra

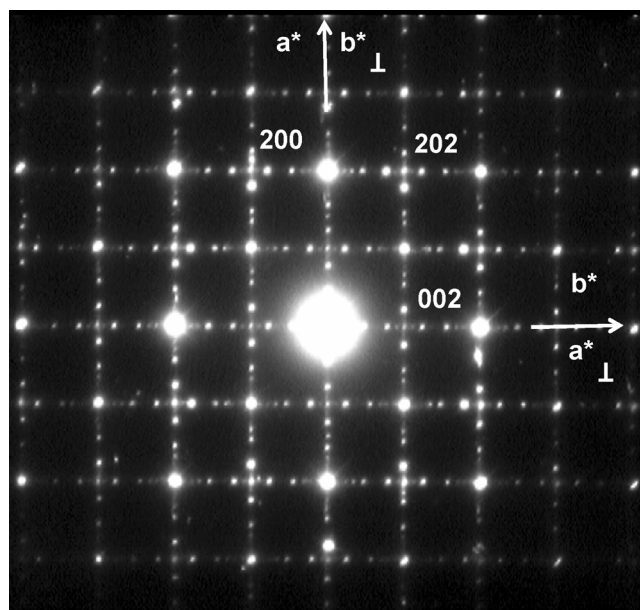


Fig. 4. Typical 010 × electron diffraction pattern of $\text{Ca}_{0.9}\text{Yb}_{0.1}\text{MnO}_{3-\delta}$ prepared by coprecipitation and SPS sintered observed on 'reduced' $\text{Ca}_{0.9}\text{Yb}_{0.1}\text{MnO}_3$ grains. Here extra spots characteristic of the substructures of the $\text{Ca}_{0.9}\text{Yb}_{0.1}\text{MnO}_{3-\delta}$ phase are clearly evidenced around the main ED spots of the nominal $\text{Ca}_{0.9}\text{Yb}_{0.1}\text{MnO}_3$ phase. This ED pattern is the result of the superposition of two 010 × ED pattern of two reduced domains disoriented from 90° one to each other.

spots is not regular compared to the periodicity of the main spots of the structure. As already mentioned in Reller et al.,¹⁸ these extra spots are representative of superstructures due to a partial reduction of the O3 nominal compound. Here the SPS treatment has probably induced a partial and not regular loss of oxygen in these grains. The original cell of the O3 nominal compound is enlarged by the distribution of the lack of oxygen involving these subcells.

This random repartition of the oxygen non-stoichiometry is responsible for all the structure defects systematically observed (Fig. 4) on some grains of these SPS treated samples. Due to the complexity of these phenomena, no systematic investigations were undertaken to really quantify these substructures.

3.3. Microstructure

The observations of starting powders (Fig. 5a and b) indicate that both morphologies are very different. The powder obtained by solid state reaction exhibits coarse 0.5–3 μm grains, while coprecipitation shows a typical aggregated nanoparticles aspect of about 100 nm. Moreover, these particles were found to be homogeneously distributed. The particle size difference between the solid state reaction and coprecipitation powder seems to be a cause of the different initial densities, and can be related to the decrease of the sintering temperature, as has been demonstrated by the shrinkage shown in Fig. 1.

Table 1 lists the densities of samples before and after sintering, with the sintering temperatures previously determined from the shrinkage curves. The relative densities are also listed.

Table 2

Lattice parameters of CaMnO_3 and $\text{Ca}_{0.9}\text{Yb}_{0.1}\text{MnO}_3$.

	Orthorhombic lattice Pnma			
	a (Å)	b (Å)	c (Å)	V (Å ³)
CaMnO_3 [17]	5.28287(5)	7.45790(7)	5.26746(5)	207.533(6)
$\text{Ca}_{0.9}\text{Yb}_{0.1}\text{MnO}_3$ [14]	5.2815(6)	7.4532(5)	5.2719(6)	207.53(1)
CS1	5308(6)	7.47(1)	5273(7)	209.0(8)
CS2	5296(2)	7466(3)	5268(3)	208.3(3)

In both case cases, the densities were close to 94% of the monocrystalline density except for the conventional sintering sample prepared by using the SSS powder.

The scanning electron micrographs of the samples with polished and quenched surfaces are shown in Fig. 5c–f. From this we can conclude that:

After sintering, the sintered sample made from both starting ‘SSS’ and ‘COP’ powders showed different grain sizes. In all

cases, the samples were found to be compact, with a good connection between the grains for both processes, CS (Fig. 5c and d) and SPS (Fig. 5e and f).

Regarding sample SPS2 (Fig. 5f), we can note that an interesting microstructure is generated after Spark Plasma Sintering showing inhibited grain growth. The sample SPS1 (Fig. 5e) prepared from the SSS powder presents a larger grain sizes and contrasted grains.

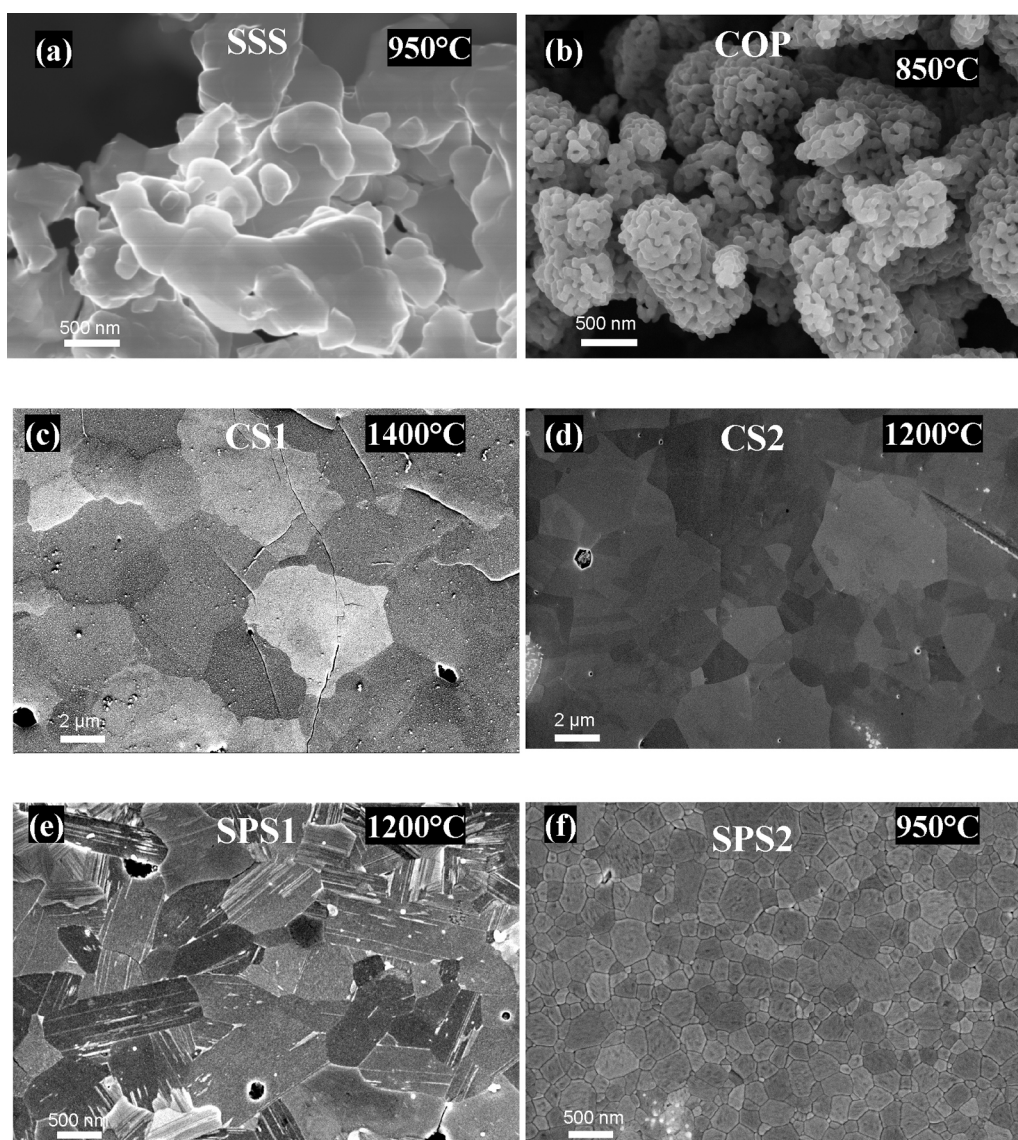


Fig. 5. SEM picture of $\text{Ca}_{0.9}\text{Yb}_{0.1}\text{MnO}_{3-\delta}$ calcined powder made by (a) solid state synthesis and (b) co-precipitation. c–f corresponds to sintered samples CS1, CS2, SPS1 and SPS2 respectively.

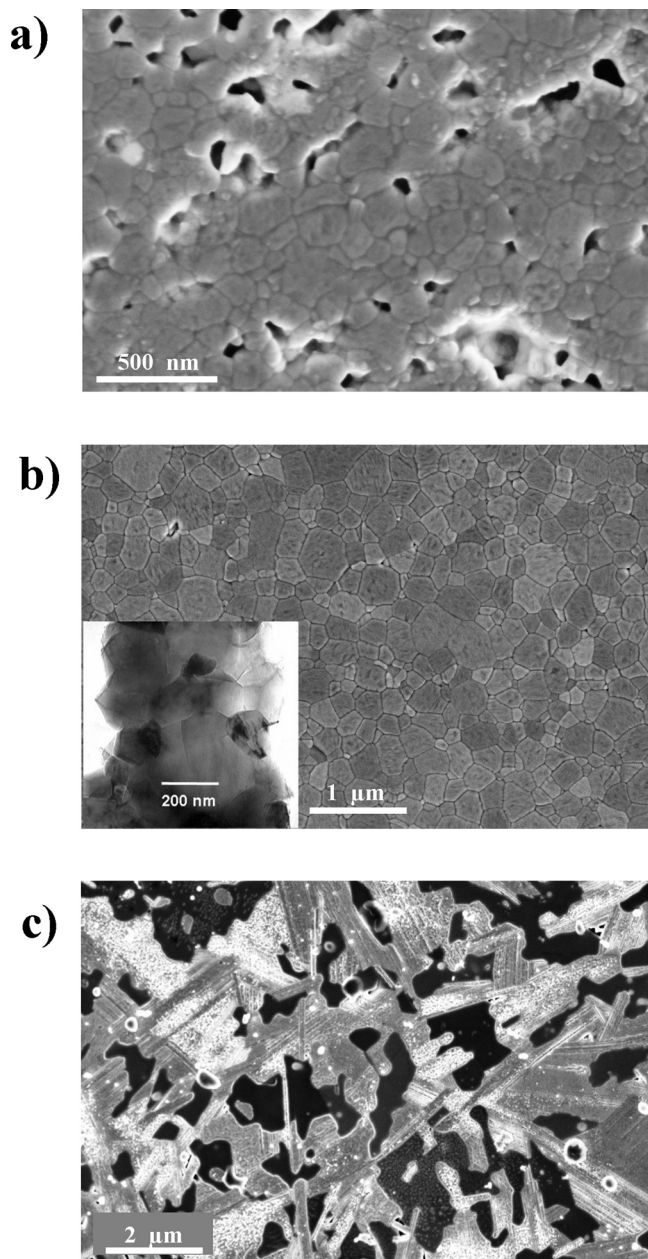


Fig. 6. SEM pictures of polished SPS prepared sample pressed at 50 MPa and sintered at 900 °C (a), 950 °C (b), and 1000 °C (c).

In Fig. 6, for both SPS and conventional sintered (CS) samples; the grain sizes are strongly correlated to the maximum sintering temperature. The amount of pores decreases until temperature reaches 950 °C, and at higher temperature the morphology and the microstructure are observed to change (Fig. 6c). This is in good agreement with the X-rays diffraction study (Fig. 3, 60 and 180 min) which showed the disappearance of the $\text{Ca}_{0.9}\text{Yb}_{0.1}\text{MnO}_{3-\delta}$ phase in favor of CaMn_2O_4 and $\text{Ca}_2(\text{MnO}_4)$. Here, this microstructure is the result of a partial decomposition and a formation of these two new phases. Hence, we can conclude that 950 °C with a dwell time of 10 min is the optimal condition for phase stability and for grain growth control by using spark plasma sintering method.

Table 3

Oxygen content of $\text{Ca}_{0.9}\text{Yb}_{0.1}\text{MnO}_{3-\delta}$ determined by titration.

Sample	Oxygen content
Powder, co-precipitation	2.93(5)
Powder, solid state synthesis	2.89(5)
Conventional sintering, co-precipitation	2.89(5)
Conventional sintering, solid state synthesis.	2.87(5)
SPS without annealing, co-precipitation	2.67(5)
SPS, coprecipitation, annealed (100 °C/min, 800 °C, 2 h)	2.79(5)

Inset Fig. 6b shows TEM observations carried out on crushed samples and confirms the average grain size (~ 250 nm) on SPS samples sintered at 950 °C. Most of the grains present a good crystallinity. As already confirmed from the ED observations, some of the grains present perturbed contrasts characteristic of the presence of important defects such as twin boundaries, substructures or strains. The reducing atmosphere combined to the high pressure applied during sintering in the SPS process is probably responsible for this typical microstructure of spark plasma sintered samples. The defects are certainly due to the partial reduction of the $\text{Ca}_{0.9}\text{Yb}_{0.1}\text{MnO}_3$ parent oxide involving the formation of $\text{Ca}_{0.9}\text{Yb}_{0.1}\text{MnO}_{3-\delta}$ with different oxygen deficient phases coexisting in the grains.

These phenomena are shown in Fig. 7. A single grain exhibiting clear evidence of a twin boundary formation, and the observed irregular contrasts are typical of those observed in the reduced $\text{CaMnO}_{3-\delta}$ compounds.¹⁸ It has to be noted that in the same grains non-stoichiometric ($\text{CaMnO}_{3-\delta}$ phase) and stoichiometric (CaMnO_3 phase) can be evidenced. Close to the grain edge the typical perovskite contrasts are observed (enlargement Fig. 7b) while the reduced phase contrasts are observed in the main body of the grain (Fig. 7a).

The measured oxygen content is presented in Table 3. On the one hand, it indicates a similar oxidation state between both SSS and COP synthesis; On the other hand, it shows an important difference between the two sintering techniques. Conventional sintering slightly reduces the oxygen content, whereas SPS induces an important oxygen deficiency. Fortunately this oxygen content can be recovered by thermal annealing in air, at 800 °C for 12 h.

3.4. Thermoelectric properties

Fig. 8a shows the temperature dependence of the resistivity for the CS (conventional sintering) and SPS (spark plasma sintering) samples respectively. The typical behavior of a semiconductor can be observed for the SPS (as-processed and annealed) samples. For the CS samples, the metallic conduction is evidenced as the electrical resistivity increases with increasing the temperature. The SPS samples have a larger ρ than the CS probably due to the higher grain boundaries densities in the case of the SPS2 sample with respect to the CS2 one. The CS curves have also been compared. The sample prepared at 1400 °C using solid state synthesis (SSS) powder shows lower resistivity values than the one prepared at 1200 °C and obtained from the

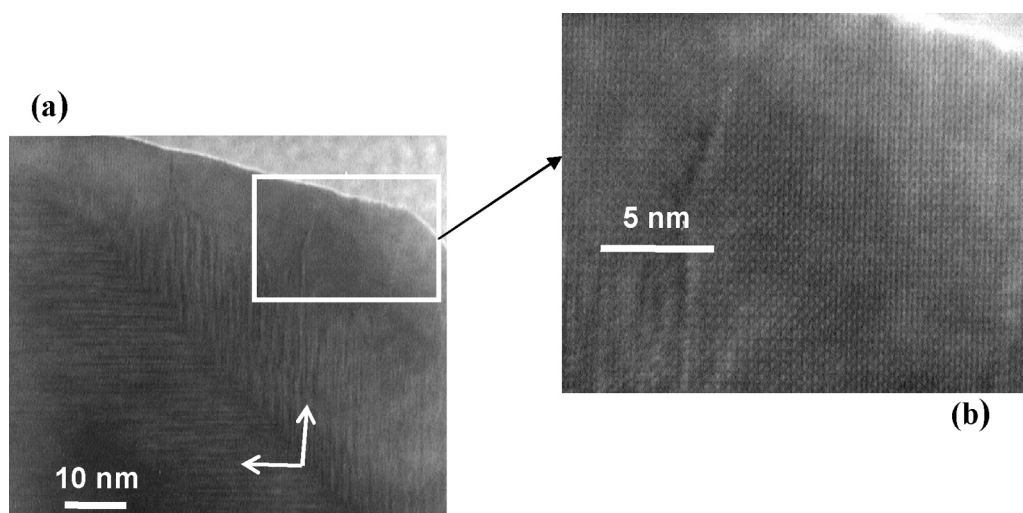


Fig. 7. SPS2 typical image presenting the contrasts resulting from the 90° disoriented domains walls (a). Grain edge observation present typical perovskite contrast (b).

co-precipitation (COP) powder. The large size of the SSS powder associated to high sintering temperature leads to the large size particles, involving fewer grain boundaries. This could explain the low resistivities.

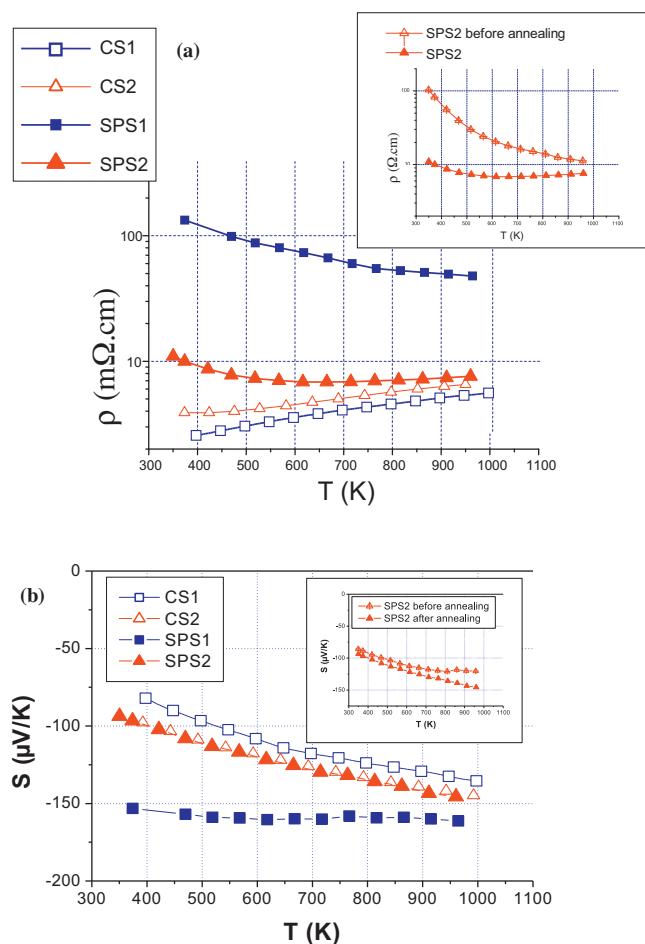


Fig. 8. Electrical resistivities (a) and Seebeck (b) coefficient of CS1, CS2, SPS1 and SPS2 samples. Inset shows SPS2 before and after annealing.

The thermopower, S (for Seebeck coefficient) confirms n -type conduction for all samples (Fig. 8b). The Seebeck values decrease in the entire temperature range. The thermopower of materials seems to be affected by the interfaces or grain boundaries; the variation in S in the sample originates: (i) from the processing condition. As already mentioned, the SPS samples were processed under dynamic vacuum, which leads to oxygen deficiency probably owing to the reduction of manganese valence from Mn^{4+} to Mn^{3+} . (ii) Intrinsic variation due to the nano or micron particle size of the samples. Such type of behavior has been reported for different sizes of nanowires of LaSrCoO_3 .¹⁹

Fig. 9 shows the thermal conductivity, κ , as a function of temperature. κ decreases with increasing temperature. Below 500 K, the particle size can be evidenced. The samples with large particle sizes show high values of κ . The low value for sample SPS2 could be explained by the finer grain size as evidenced in

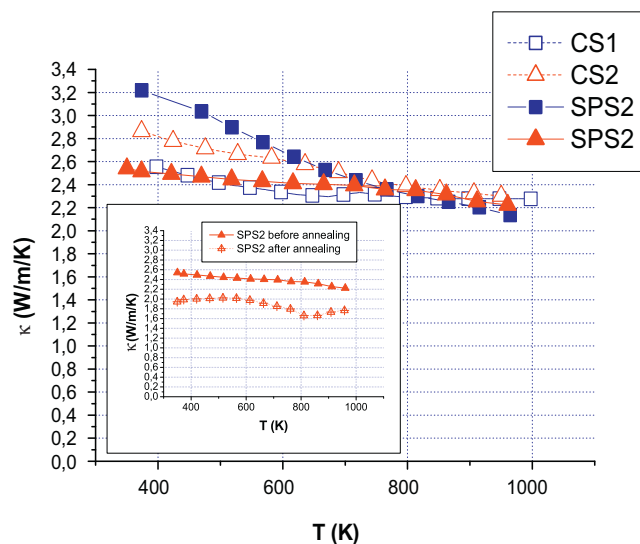


Fig. 9. Thermal conductivities of CS1, CS2, SPS1 and SPS2 samples. Inset, SPS2 before and after annealing.

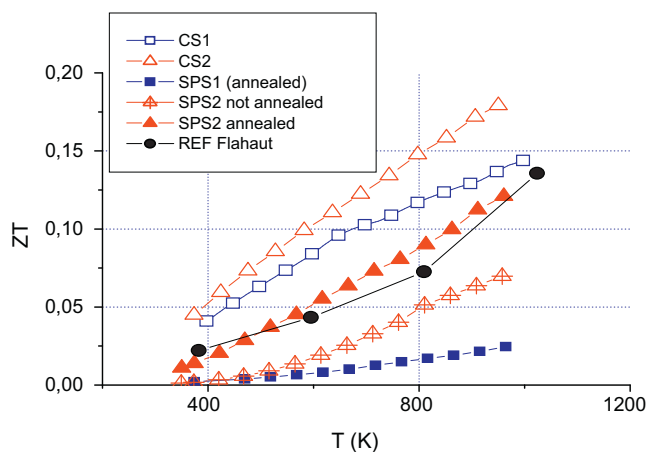


Fig. 10. Figure of merit of CS1, CS2, SPS1 and SPS2 samples before and after annealing. Ref. from Flahaut et al.²⁰

Fig. 5f. On the other hand, the lower thermal conductivity, κ , for CS1 seems to be related to the sample density. After 500 K, the effect of the processing condition of particle size seems to be neglected.

Dimensionless figure of merit (ZT) for all samples is shown in Fig. 10. These results indicate that the value of ZT increases monotonically with temperature. Basically, the ZT is improved for the sample showing the fine particle with the best performance of $ZT = 0.18$ at 750°C for CS2 comparable with the results reported elsewhere.²⁰

4. Conclusion

The goal of this study is to propose a new way of processing of n -type thermoelectric oxides. We demonstrated that by using co-precipitation synthesis, we can prepare a finer and homogeneous powder, without using complex chemicals. Structure analysis confirms the formation of $\text{Ca}_{0.9}\text{Yb}_{0.1}\text{MnO}_3$ with high density at a temperature of 950°C , i.e. 200°C lower than in the case of conventional processing. The samples obtained show better thermoelectric results than the conventional synthesis route. The figure of merit, ZT , reaches 0.18 at 750°C . Moreover the non-conventional spark plasma sintering has been used to control the grain growth during processing.

Acknowledgments

S. Quétel-Weben acknowledge fellowship from “Ministère Français de la Recherche et de la Technologie”, In addition,

the authors acknowledge FEDER, CNRS and CRBN for their financial participation (CPER 2007–2013) to the experimental set-up used in this work.

References

1. Ioffe AF. *Semiconductor thermoelements, and thermoelectric cooling*. London: Infosearch, Ltd; 1957.
2. Rosi FD. Thermoelectricity and thermoelectric power generation. *Solid State Electron* 1968;**11**:833–68.
3. Yang J, Caillat T. Thermoelectric materials for space and automotive power generation. *MRS Bull* 2006;**31**:224–9.
4. Terasaki I, Sasago Y, Uchinokura K. Large thermoelectric power in NaCo_2O_4 single crystals. *Phys Rev B* 1997;**56**:R12685–7.
5. Heller MW. Electrical transport properties of SiGe thermoelectric alloys doped with As, P, and As+P. *J App Phys* 1976;**47**:4113.
6. Mahan GD. Good thermoelectrics. *Solid State Phys* 1997:81–157.
7. Masset A, Michel C, Maignan A, Hervieu M, Toulemonde O, Studer F, et al. Misfit-layered cobaltite with an anisotropic giant magnetoresistance: $\text{Ca}_3\text{Co}_4\text{O}_9$. *Phys Rev B* 2000;**62**:166–75.
8. Noudem JG, Lemonnier S, Prevel M, Reddy ES, Guilmeau E, Goupil C. Thermoelectric ceramics for generators. *J Eur Ceram Soc* 2008;**28**: 41–8.
9. Noudem JG, Kenfaui D, Quétel-Weben S, Sanmathi CS, Retoux R, Gomina M. Spark plasma sintering of n -type thermoelectric $\text{Ca}_{0.95}\text{Sm}_{0.05}\text{MnO}_3$. *J Am Ceram Soc* 2011;**94**:2608–12.
10. Bérardan D, Guilmeau E, Maignan A, Raveau B. $\text{In}_2\text{O}_3\text{:Ge}$ a promising n -type thermoelectric oxide composite. *Solid State Commun* 2008;**146**:97–101.
11. Muta H, Kurosaki K, Yamanaka S. Thermoelectric properties of rare earth doped SrTiO_3 . *J Alloy Compd* 2003;**350**:292–5.
12. Ohtaki M, Araki K, Yamamoto K. High thermoelectric performance of dually doped ZnO ceramics. *J Electron Mater* 2009;**38**:1234–8.
13. Wang Y, Sui Y, Fan H, Wang X, Su Y, Su W, et al. High temperature thermoelectric response of electron-doped CaMnO_3 . *Chem Mater* 2009;**21**:4653–60.
14. Wang Y, Sui Y, Su W. High temperature thermoelectric characteristics of $\text{Ca}_{0.9}\text{R}_{0.1}\text{MnO}_3$ ($R = \text{La, Pr, ... , Yb}$). *J App Phys* 2008;**104**:093703.
15. Flahaut D, Mihara T, Funahashi R, Nabeshima N, Lee K, Ohta H, et al. Thermoelectrical properties of A-site substituted $\text{Ca}_{1-x}\text{Re}_x\text{MnO}_3$ system. *J Appl Phys* 2006;**100**:084911.
16. Sanmathi CS, Takahashi Y, Sawaki D, Klein Y, Retoux R, Terasaki I, et al. Microstructure control on thermoelectric properties of $\text{Ca}_{0.96}\text{Sm}_{0.04}\text{MnO}_3$ synthesised by co-precipitation technique. *Mater Res Bull* 2010;**45**: 558–63.
17. Zhou Q, Kennedy BJ. Thermal expansion and structure of orthorhombic CaMnO_3 . *J Phys Chem Solids* 2006;**67**:1595–8.
18. Reller A, Thomas JM, Jefferson DA, Uppal MK. Superstructures formed by the ordering of vacancies in a selective oxidation catalyst: grossly defective CaMnO formula. *P Roy Soc A Math Phys* 1984;**394**:223–41.
19. Wang Y, Fan HJ. Improved thermoelectric properties of $\text{La}_{1-x}\text{Sr}_x\text{CoO}_3$ nanowires. *J Phys Chem C* 2010;**114**:13947–53.
20. Flahaut D, Funahashi R, Lee K, Ohta H, Koumoto K. Effect of the Yb substitutions on the thermoelectric properties of CaMnO_3 . Vienna: ICT 2006. *Int Conf Thermoelect* 2006:103–6.